Journal of Power Sources 246 (2014) 887–898

Contents lists available at ScienceDirect

Journal of Power Sources

journal homepage: www.elsevier.com/locate/jpowsour

First-principles thermal modeling of electric double layer capacitors under constant-current cycling

Anna d'Entremont, Laurent Pilon*

University of California, Los Angeles, Henry Samueli School of Engineering and Applied Science, Mechanical and Aerospace Engineering Department, 420 Westwood Plaza, Los Angeles, CA 90095, USA

HIGHLIGHTS

- New thermal model for EDLCs was rigorously derived from first principles.
- Irreversible and reversible contributions to heat generation were accounted for and physically interpreted.
- Spatiotemporal variations of heat generation rates and temperature were investigated.
- Simulations qualitatively reproduced experimental temperature measurements under various conditions.

GRAPHICAL ABSTRACT

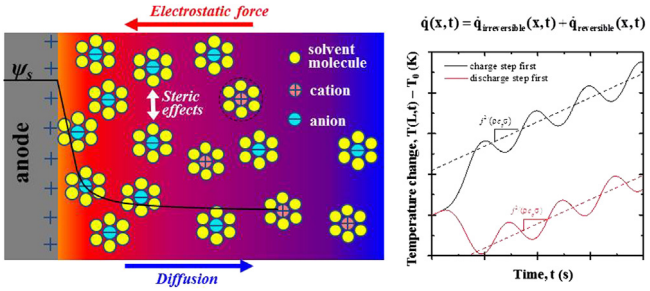

ARTICLE INFO

Article history:
Received 17 May 2013
Received in revised form
7 August 2013
Accepted 10 August 2013
Available online 19 August 2013

Keywords:
Supercapacitors
Energy storage
Joule heating
Reversible heating
Heat transfer

ABSTRACT

This study aims to develop physical modeling and understanding of the coupled electrodiffusion, heat generation, and thermal transport occurring in electric double layer capacitors (EDLCs) during constant-current cycling. To do so, the governing energy equation was derived from first principles and coupled with the modified Poisson–Nernst–Planck model for transient electrodiffusion in a binary and symmetric electrolyte. In particular, irreversible Joule heating and reversible heat generation rates due to ion diffusion, steric effects, and changes in entropy of mixing in EDLCs were rigorously formulated. Detailed numerical simulations of the temperature rise in the electrolyte were performed for planar electrodes. The results qualitatively reproduced experimental data reported in the literature under various charging/discharging conditions.

1. Introduction

Electric double layer capacitors (EDLCs) are promising electrical energy storage devices. They store electric charge physically within the electric double layer forming at the mesoporous electrode/electrolyte interface. They fill the gap between batteries featuring high energy densities but low power densities and conventional dielectric capacitors offering high power densities but low energy densities [1,2]. EDLCs offer significantly larger power densities, longer cycle life, and higher cycle efficiencies than batteries, while still offering higher energy densities than conventional capacitors [1–5]. Their high power capability, rapid cycling, and long cycle life make them attractive for applications such as load leveling, regenerative braking, and dynamic stabilization of the utility grid [1–5]. Recovering energy from intermittent environmental sources of thermal, mechanical, and photon energy is also a potential application for EDLCs [1].

* Corresponding author. Tel.: +1 (310) 206 5598; fax: +1 (310) 206 2302.
E-mail address: pilon@seas.ucla.edu (L. Pilon).

0378-7753/$ – see front matter © 2013 Elsevier B.V. All rights reserved.
http://dx.doi.org/10.1016/j.jpowsour.2013.08.024

During EDLC charging and discharging, a portion of the electrical energy is lost as heat. The heat generation rate depends on the cell design, its materials, and its operating conditions [3]. Elevated temperatures result in (i) accelerated aging of EDLCs [2–7], (ii) increased self-discharge rates [2,4–6], (iii) increased cell pressure, and possibly (iv) electrolyte evaporation [6]. As EDLCs age, their resistance increases and their capacitance decreases in, which in turn leads to higher cell temperature and voltage [7]. In addition, temperature differences between series-connected EDLCs can cause voltage imbalances and destructive overvoltage of individual cells [2,3]. To avoid these harmful effects, temperature changes in EDLCs should be mitigated. To do so, thermal modeling can be used (i) to predict operating temperatures and develop thermal management strategies for existing EDLC designs and (ii) to predict the thermal behavior of novel EDLC designs.

This study aims to develop physical modeling and understanding of the coupled electrodiffusion, heat generation, and thermal transport occurring in electric double layer capacitors during operation. To do so, governing equations were derived and detailed numerical simulations of planar electrodes were developed and qualitatively compared with experimental data reported in the literature. In particular, irreversible and reversible heat generation rates and temperature rise in EDLCs were investigated for the practical case of constant-current cycling.

2. Background

2.1. Structure of the electric double layer

Fig. 1 illustrates the electric double layer (EDL) forming near a planar electrode. The Stern model [8,9] proposes that the EDL within the electrolyte consists of the Stern and diffuse layers. The Stern layer is defined as the compact layer near the electrode surface with no free charge [8,9]. By contrast, ions in the diffuse layer are mobile under the coupled influences of electrostatic forces and diffusion [8,9]. The overall thickness of the EDL varies with potential and concentration [8,9].

2.2. Models for time-dependent ion transport

The Poisson–Nernst–Planck (PNP) model describes time-dependent electrodiffusion in the diffuse layer. The Poisson equation governs the local electric potential ψ, while the Nernst–Planck equations describe the ion transport. The Nernst–Planck equations are based on the dilute solution theory and treat ions as non-interacting point charges. Thus, there is no upper limit to the ion concentrations at the electrode surface [10]. This reduces the validity of the PNP model to dilute electrolytes subjected to low surface potentials. In fact, the PNP model predicts surface ion concentrations larger than the theoretical maximum concentration c_{max} for surface potentials only a few times larger than the thermal voltage $\psi_T = R_u T/zF$ [10]. Here, R_u is the universal gas constant, T is the absolute temperature, F is the Faraday constant, and z is the ion valency. Assuming simple cubic packing, c_{max} can be expressed as $c_{max} = 1/N_A a^3$ where a is the effective ion diameter and N_A is the Avogadro constant [10].

Recently, Kilic et al. [10] derived a modified Poisson-Nernst-Planck (MPNP) model accounting for the finite ion size and valid for large electrolyte concentrations and surface potentials. The model was derived for binary and symmetric electrolytes with constant permittivity. This MPNP model will be used in the present study.

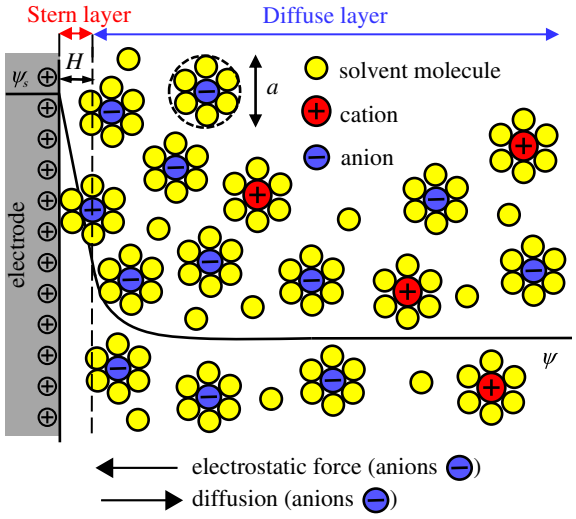

Fig. 1. Illustration of electric double layer structure near a planar electrode.

2.3. Experimentally-observed thermal behavior of EDLCs

Experimental studies have shown that constant-current cycling of EDLCs under current $\pm I_s$ resulted in an overall rise in temperature from cycle to cycle with superimposed temperature oscillations at the cycle frequency [3–6,11–13]. The overall temperature rise corresponded to irreversible heating and was proportional to I_s^2 [4]. The temperature oscillations were attributed to reversible heating which was exothermic during charging, endothermic during discharging, and proportional to I_s [4,11,12]. Finally, the amplitude of the temperature oscillations at the EDLC outer surface increased with increasing potential window and with decreasing current [4].

2.4. Thermal modeling of EDLCs

Existing thermal models of EDLCs predicted the EDLC temperature as a function of space and/or time. They solved the heat diffusion equation within the cell [2,5,13] or employed the thermal circuit analogy [2,6]. The irreversible heat generation rate was either imposed as an input parameter [2,5,11] or predicted as Joule heating using the imposed current and the experimentally-measured resistance of the device [4,6,7]. It was also assumed to be uniform throughout the entire device [5,6,11,13] or to have different values in the current collectors, electrodes, and separator [2].

Most models predicted the overall temperature rise, but failed to account for the reversible heat generation and to predict the temperature oscillations [2,5,6,11]. To the best of our knowledge, the only existing model of EDLC reversible heating was developed by Schiffer et al. [4]. The authors considered that the entropy of the ions (i) decreased during charging as ions formed the EDL and (ii) increased during discharging as they returned to their uniform concentration [4]. These processes were respectively exothermic and endothermic to satisfy the second law of thermodynamics [4]. The entropy change ΔS of the ions due to EDL formation in a binary electrolyte with identical ion size was estimated as [4]

$$\Delta S = 2k_B \ln\left(\frac{V_S}{V_0}\right)^N. \quad (1)$$

Here, k_B is the Boltzmann constant, $N \approx C_i\psi_s/e$ is the number of ions in each EDL for monovalent electrolyte, e is the elementary charge, and ψ_s is the cell voltage. The ions were assumed to occupy the total electrolyte volume V_0 in the discharged state and the Stern layer volume V_S in the charged state. The differential capacitance C_i was

such that $C_i d\psi_s/dt = I_s$ [4]. The reversible heat generation rate $\dot{Q}_{rev,S}$ (in W) was then predicted as [4]

$$\dot{Q}_{rev,S} = -T\frac{dS}{dt} = -2T\frac{k_B}{e}\ln\left(\frac{V_S}{V_0}\right)C_i\frac{d\psi_s}{dt} = -2\frac{Tk_B}{e}\ln\left(\frac{V_S}{V_0}\right)I_s(t) \tag{2}$$

where T is the average cell temperature and S is the entropy of the EDLC system. This expression indicates that $\dot{Q}_{rev,S}$ is proportional to the current, as observed experimentally [12]. However, the derivation assumed that the EDL consisted of a monolayer of ions and that the capacitance was independent of cell voltage. Actual EDLCs are known to violate these assumptions [8,9]. In addition, Equation (2) predicts the overall reversible heat generation rate for the entire device and ignores its spatial variation. It was also difficult to validate experimentally due to large uncertainties in evaluating V_S and V_0 for porous electrodes. Instead, Schiffer et al. [4] fitted the value of $\ln(V_S/V_0)$ using the measured temperature oscillation amplitude and compared it with an estimate based on the device geometry. Equation (2) was later used in two semi-empirical thermal models [7,13]. Gualous et al. [13] found good agreement between their temperature predictions and experimental measurements. However, the details of how they implemented $\dot{Q}_{rev,S}$ and evaluated V_S and V_0 remain unclear.

Existing thermal models of EDLCs predicted total irreversible and reversible heat generation rates for entire devices. They assumed uniform heat generation and relied on experimentally-measured device properties including electrical resistance. They did not account for the detailed physical phenomena in EDLCs such as electric double layer formation and ion transport. Unfortunately, these models can neither predict the thermal performance of novel and untested EDLC designs, nor predict how different device designs and materials would affect the heat generation and temperature.

The present study develops a spatiotemporal physical model accounting for coupled ion transport, heat generation, and thermal transport during operation of a planar EDLC. The heat generation rates within the electrolyte were derived from first principles. This model was used to understand the physical phenomena governing the local thermal behavior of EDLCs and to address several fundamental questions, namely (i) what physical processes account for the experimentally-observed temperature oscillations? (ii) Does the heat generation rate vary significantly with space and/or time? (iii) Are the assumptions used by current thermal models appropriate?

3. Analysis

3.1. Schematic and assumptions

Fig. 2 schematically shows a one-dimensional cell of thickness $2L$ consisting of two planar electrodes separated by liquid electrolyte. The electrode located at $x = 0$ will be denoted by electrode A and the electrode at $x = 2L$ by electrode B. The electrolyte consists of three regions: a Stern layer adjacent to each electrode and one diffuse layer. The EDLC is charged and discharged under current density $j_s(t)$ imposed at electrode A.

To make the problem mathematically tractable, the following assumptions were made: (1) chemical reactions and ion insertion into the electrode were absent. (2) The electrolyte was binary and symmetric, i.e., it consisted of two ion species with identical valency z, diffusion coefficient D, and effective diameter a. (3) Dissociation of the electrolyte was complete. (4) Bulk movement of the electrolyte, i.e., advection, was negligible. (5) All electrolyte properties were constant and independent of temperature, with the sole exception of the concentration-dependent electrical conductivity of the electrolyte. (6) The simulated EDLC was thermally insulated, and (7) the Stern layer thickness H was assumed to be equal to half of the effective ion diameter, i.e., $H = a/2$.

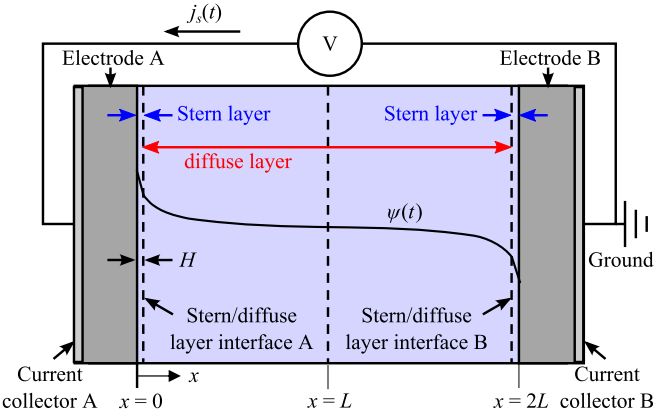

Fig. 2. Illustration of simulated 1D cell.

Assumptions (1)–(3) are realistic for typical EDLC devices using, for example, aqueous KOH or $TEABF_4$ in acetonitrile as electrolyte [4,14]. Bazant et al. [15] suggested that the assumption of symmetric ion size is reasonable for solvated ions since smaller bare ions tend to be more solvated than larger ions. Assumption (4) is satisfied if the electrolyte is confined in a porous separator inhibiting bulk fluid motion [2,5,16]. Assumptions (5) and (6) are appropriate first order approximations for relatively small temperature variations. However, the effects of temperature on the electrolyte properties and ion transport are expected to become significant for large temperature rises. These assumptions will be relaxed in future studies.

3.2. Poisson equation

3.2.1. Formulation

The equation governing the electric potential $\psi(\mathbf{r},t)$ at location $\mathbf{r}$ and time t is the Poisson equation expressed as [10,17,18]

$$\nabla\cdot(\varepsilon_0\varepsilon_r\nabla\psi) = \begin{cases} 0 & \text{in the Stern layers} \\ -F\sum_{i=1}^{n} z_i c_i & \text{in the diffuse layer} \end{cases} \tag{3}$$

where $c_i(\mathbf{r},t)$ and z_i respectively denote the concentration and valency of species i and n is the number of ion species present. For binary and symmetric electrolytes, $n = 2$ and $z_1 = -z_2$. Here, ε_0 and ε_r are the vacuum permittivity and the relative permittivity of the electrolyte, respectively. The Faraday constant is denoted by F. The Stern layers contain no free charges and the electric potential profile is linear.

3.2.2. Boundary and initial conditions

The one-dimensional Poisson Equation (3) in Cartesian coordinates governing $\psi(x,t)$ is a second-order partial differential equation (PDE) in space. It is solved within both the Stern and the diffuse layers. Two boundary conditions are required for each region. Here, the initial potential was assumed to be uniform and equal to zero, i.e.,

$$\psi(x,0) = 0\,\text{V} \quad \text{for } 0 \le x \le 2L. \tag{4}$$

The current density at the surface of electrode A at $x = 0$ was imposed as a square wave of period t_c alternating between j_s

and $-j_s$. The imposed current corresponds to an electronic current in the external circuit which induces an ion flux within the electrolyte. The boundary condition at the surface of electrode A corresponds to charge conservation across the electrode/electrolyte interface so that the displacement current j_{disp} matches the imposed electronic current j_s, i.e.,

$$j_{\text{disp}} = -\varepsilon_0\varepsilon_r\frac{\partial^2\psi}{\partial t\partial x}(0,t) = \begin{cases} j_s & \text{for } (n_c-1)t_c \le t < (n_c-1/2)t_c \\ -j_s & \text{for } (n_c-1/2)t_c \le t < n_c t_c \end{cases} \tag{5}$$

where j_s is the magnitude of the imposed current density and n_c is the cycle number $n_c = 1,2,\ldots$. In addition, the electric potential and electric displacement were continuous across the Stern/diffuse layer interface located at $x = H$ so that [17–19],

$$\psi\left(H^-,t\right) = \psi\left(H^+,t\right) \quad \text{and} \quad \varepsilon_0\varepsilon_r\frac{\partial\psi}{\partial x}\left(H^-,t\right) = \varepsilon_0\varepsilon_r\frac{\partial\psi}{\partial x}\left(H^+,t\right). \tag{6}$$

Similarly, the electric potential and electric displacement were continuous across the second Stern/diffuse layer interface located at $x = 2L - H$, i.e., [17–19],

$$\begin{aligned} &\psi\left(2L-H^-,t\right) = \psi\left(2L-H^+,t\right) \quad \text{and} \\ &\varepsilon_0\varepsilon_r\frac{\partial\psi}{\partial x}\left(2L-H^-,t\right) = \varepsilon_0\varepsilon_r\frac{\partial\psi}{\partial x}\left(2L-H^+,t\right). \end{aligned} \tag{7}$$

Furthermore, the electrical ground was defined at the surface of electrode B, located at $x = 2L$, i.e.,

$$\psi(2L,t) = 0V. \tag{8}$$

The choice of reference potential is arbitrary and affects neither ion transport nor heat transfer.

3.3. Mass conservation equation

3.3.1. Formulation

In the diffuse layer, the concentrations $c_1(\mathbf{r},t)$ and $c_2(\mathbf{r},t)$ satisfy the mass conservation equation given by [10]

$$\frac{\partial c_i}{\partial t} = -\nabla\cdot\mathbf{N_i} \quad \text{for } i = 1,2,\ldots,n \tag{9}$$

where $\mathbf{N}_i(\mathbf{r},t)$ is the local flux of species i. For a binary ($n = 2$) and symmetric electrolyte, the ion flux $\mathbf{N}_i(\mathbf{r},t)$ is expressed as [10]

$$\mathbf{N}_i(\mathbf{r},t) = -\left[D\nabla c_i + \frac{z_i FD}{R_u T}c_i\nabla\psi + \frac{Da^3N_Ac_i}{1-a^3N_A(c_1+c_2)}\nabla(c_1+c_2)\right] \tag{10}$$

where D is the ion diffusion coefficient in the electrolyte and a is the effective ion diameter. Here, R_u is the universal gas constant $R_u = 8.314$ J mol^{-1} K^{-1} and N_A is the Avogadro constant $N_A = 6.022\times10^{23}$ molecules mol^{-1}. The first and second terms on the right-hand side of Equation (10) represent the ion fluxes due to diffusion and migration in an electric field, respectively [20]. The third term accounts for steric effects caused by finite ion size [10]. In particular, it ensures that the total ion concentration $c_1 + c_2$ cannot exceed the theoretical maximum concentration $c_{\max} = 1/N_Aa^3$ corresponding to ion close packing. The electric potential and ion transport governed by Equations (3), (9) and (10) are coupled to the thermal behavior through the local temperature T in Equation (10) and through the temperature dependence of the diffusion coefficient D and relative permittivity ε_r.

3.3.2. Boundary and initial conditions

The one-dimensional mass conservation Equation (9) in Cartesian coordinates is a first order PDE in terms of time and second order in space. It is solved within the diffuse layer only. It requires one initial condition and two boundary conditions for the concentration $c_i(x,t)$ of each ion species. Both species of the binary and symmetric electrolyte were assumed to start at the same uniform bulk concentration c_∞ such that

$$c_1(x,0) = c_2(x,0) = c_\infty \quad \text{for } 0 \le x \le 2L. \tag{11}$$

As previously mentioned, ion insertion into the electrode was ignored, so the ion flux at the Stern/diffuse layer interface located at $x = H$ vanished, i.e.,

$$N_1(H,t) = N_2(H,t) = 0 \text{ mol m}^{-2}\text{s}^{-1}. \tag{12}$$

Similarly, the ion flux vanished at the second Stern/diffuse layer interface located at $x = 2L - H$, i.e.,

$$N_1(2L-H,t) = N_2(2L-H,t) = 0 \text{ mol m}^{-2}\text{s}^{-1}. \tag{13}$$

3.4. Energy conservation equation

3.4.1. Formulation

Applying energy conservation principles to a fixed control volume of electrolyte in the absence of bulk motion and chemical reactions yields the following energy conservation equation [21]

$$\frac{\partial}{\partial t}(\rho u) = -\nabla\cdot\mathbf{q}'' \tag{14}$$

where $\rho(\mathbf{r},t)$ is the electrolyte density, $u(\mathbf{r},t)$ is the specific internal energy of the electrolyte, and $\mathbf{q}''(\mathbf{r},t)$ is the local energy flux at location $\mathbf{r}$ and time t. For a multicomponent system with concentration gradients, the energy flux $\mathbf{q}''$ includes contributions from Fourier heat conduction, interdiffusion of species, and the Dufour effect [20,21]. The Dufour or diffusion thermo-effect refers to an energy flux driven by a gradient of electrochemical potential or pressure [22]. It is the reverse of the Soret effect or thermal diffusion [22]. The contribution from the Dufour effect is usually negligible [20–22] and will not be included here. Thus, the energy flux can be expressed as [20,21]

$$\mathbf{q}'' = -k\nabla T + \sum_{i=0}^{n}\overline{H}_i\mathbf{N}_i. \tag{15}$$

where k is the electrolyte thermal conductivity, $\overline{H}_i$ is the partial molar enthalpy of species i (in J mol^{-1}), n is the number of ion species, and subscript $i = 0$ refers to the solvent. Substituting Equation (15) into Equation (14) and using the mass conservation Equation (9) yields

$$\frac{\partial}{\partial t}(\rho u) = \nabla\cdot(k\nabla T) + \sum_{i=0}^{n}\overline{H}_i\frac{\partial c_i}{\partial t} - \sum_{i=0}^{n}\mathbf{N}_i\cdot\nabla\overline{H}_i. \tag{16}$$

The first, second, and third terms on the right-hand side of Equation (16) represent the net increase of energy within the control volume due to (i) heat conduction, (ii) accumulation of ions and/or solvent molecules, and (iii) flow of ions and/or solvent to regions with lower $\overline{H}_i$, respectively.

The energy balance given by Equation (16) can be transformed into a thermal energy balance in terms of local temperature $T(\mathbf{r},t)$. First, the change in ρu can be expressed in terms of the enthalpy per unit volume, defined by ρh, as

$$\frac{\partial}{\partial t}(\rho u) = \frac{\partial}{\partial t}(\rho h) - \frac{\partial p}{\partial t} \tag{17}$$

where $h(\mathbf{r},t)$ and $p(\mathbf{r},t)$ are respectively the specific enthalpy of the electrolyte in J kg^{-1} and the pressure in Pa at location $\mathbf{r}$ and time t. The term $\partial(\rho h)/\partial t$ can be expanded further. The exact differential of the enthalpy per unit volume, defined as ρh, of an n-component mixture can be expressed as [23]

$$\mathrm{d}(\rho h) = \rho c_p \mathrm{d}T + \left[1 + \left(\frac{\partial \ln \rho}{\partial \ln T}\right)_{p,c_i}\right]\mathrm{d}p + \sum_{i=0}^{n} \overline{H}_i \mathrm{d}c_i \tag{18}$$

where c_p is the specific heat of the electrolyte in J kg^{-1} K^{-1}. Typically $(\partial \ln \rho/\partial \ln T)_{p,c_i} \ll 1$ for liquids and solids [23]. Then, combining Equations (17) and (18) yields

$$\frac{\partial}{\partial t}(\rho u) = \rho c_p \frac{\partial T}{\partial t} + \sum_{i=0}^{n} \overline{H}_i \frac{\partial c_i}{\partial t}. \tag{19}$$

The first and second terms on the right-hand side of Equation (19) represent the time rates of change of the thermal energy and of the electrochemical potential energy, respectively. Combining Equation (19) with Equation (16) yields the energy conservation equation for the electrolyte

$$\rho c_p \frac{\partial T}{\partial t} = \nabla \cdot (k \nabla T) + \dot{q}. \tag{20}$$

This expression corresponds to the heat diffusion equation [24] where the heat generation rate $\dot{q}$ is expressed as

$$\dot{q} = -\sum_{i=0}^{n} \mathbf{N}_i \cdot \nabla \overline{H}_i. \tag{21}$$

3.4.2. Heat generation rate

The partial molar enthalpy $\overline{H}_i$ of species i can be expressed as a function of the electrochemical potential $\tilde{\mu}_i$ and the partial molar enthalpy $\overline{S}_i = -\partial \mu_i/\partial T$ according to [23]

$$\overline{H}_i = \tilde{\mu}_i + T\overline{S}_i. \tag{22}$$

The electrochemical potential $\tilde{\mu}_i = z_i F \psi + \mu_i$ of species i accounts for the electrical potential energy $z_i F \psi$ of charged species as well as for the chemical potential $\mu_i = \mu_i^0(T) + R_u T \ln(a_i)$ [20,23]. Here, $\mu_i^0(T)$ is the chemical potential of species i at a standard state and is a function of T only, while a_i is the local thermodynamic activity of species i [20,23]. Thus, the gradient $\nabla \overline{H}_i$ can be written as

$$\nabla \overline{H}_i = z_i F \nabla \psi + \nabla \mu_i + \nabla\left(T\overline{S}_i\right). \tag{23}$$

Finally, substituting Equation (23) and the expressions for the chemical potential μ_i and the partial molar entropy $\overline{S}_i$ into Equation (21), the heat generation rate $\dot{q}$ can be written as

$$\dot{q} = \dot{q}_E + \dot{q}_S = -\nabla \psi \cdot \left(\sum_{i=1}^{n} z_i F \mathbf{N}_i\right) + \sum_{i=0}^{n} \mathbf{N}_i \cdot R_u \nabla\left(T^2 \frac{\partial \ln a_i}{\partial T}\right). \tag{24}$$

The first term $\dot{q}_E$ on the right-hand side of Equation (24) represents the thermal energy released as ions decreased their electrical potential energy. Summation is carried out over the n charged ion species i, with $z_0 = 0$ for the neutral solvent. The second term $\dot{q}_S$ is the net contribution to the heat generation rate due to the gradients of chemical potential, partial molar entropy, and temperature. Heat is released as ions and/or solvent molecules decrease their entropy, as suggested by Schiffer et al. [4].

Electrical Heating. The term $\dot{q}_E$ can alternatively be written as $\dot{q}_E = \mathbf{j} \cdot \mathbf{E}$ where $\mathbf{E} = -\nabla \psi$ is the electric field vector and the ionic current density vector $\mathbf{j}$ is defined as [20]

$$\mathbf{j}(\mathbf{r},t) = \sum_{i=1}^{n} z_i F \mathbf{N}_i(\mathbf{r},t). \tag{25}$$

This term corresponds to conversion of electrical energy into thermal energy [25]. For conductors obeying Ohm's law, the current density $\mathbf{j}$ is directly proportional to the electric field, i.e., $\mathbf{j} = \sigma \mathbf{E}$, where σ is the electrical conductivity of the conductor [26]. In that case, the electrical heat generation rate can be expressed as $\dot{q}_E = \mathbf{j} \cdot \mathbf{E} = |\mathbf{j}|^2/\sigma$. This heat generation rate is irreversible and known as Joule heating [20,27,28]. However, in electrolyte with non-uniform ion concentrations, the current density depends not only on the electric field but also on diffusion and steric effects. For a binary and symmetric electrolyte with cations referred to by $i = 1$ and anions by $i = 2$, the local ionic current density $\mathbf{j}$ can be expressed, by combining Equations (10) and (25), as

$$\mathbf{j} = \sigma \mathbf{E} - DzF\nabla(c_1 - c_2) - \frac{DzFa^3 N_A(c_1 - c_2)}{1 - a^3 N_A(c_1 + c_2)} \nabla(c_1 + c_2). \tag{26}$$

In other words, electrolytes obey Ohm's law only in the absence of ion concentration gradients. The electrolyte electrical conductivity σ depends on the local ion concentrations and can be expressed as [20,29]

$$\sigma(\mathbf{r},t) = \frac{D}{R_u T} \sum_{i=1}^{n} z_i^2 F^2 c_i(\mathbf{r},t). \tag{27}$$

After some manipulations, Equation (26) can be used to express the electric field vector $\mathbf{E}$ and substitute it in the expression of the electrical heat generation rate $\dot{q}_E$. Then, for an electrolyte, $\dot{q}_E$ can be written as the sum of three contributions $\dot{q}_E(\mathbf{r},t) = \dot{q}_{E,j}(\mathbf{r},t) + \dot{q}_{E,d}(\mathbf{r},t) + \dot{q}_{E,s}(\mathbf{r},t)$. The heat generation rates $\dot{q}_{E,j}$, $\dot{q}_{E,d}$, and $\dot{q}_{E,s}$ correspond to the contributions of Joule heating, ion diffusion, and steric effects, respectively. These three contributions are expressed as

$$\dot{q}_{E,j}(\mathbf{r},t) = \frac{|\mathbf{j}|^2}{\sigma}, \quad \dot{q}_{E,d}(\mathbf{r},t) = \frac{DzF}{\sigma}\mathbf{j} \cdot \nabla(c_1 - c_2), \quad \text{and}$$
$$\dot{q}_{E,s}(\mathbf{r},t) = \frac{DzFa^3 N_A(c_1 - c_2)}{\sigma\left[1 - a^3 N_A(c_1 + c_2)\right]}\mathbf{j} \cdot \nabla(c_1 + c_2). \tag{28}$$

If the ion concentrations $c_i(\mathbf{r},t)$ are uniform or if the concentration gradients are perpendicular to the current density $\mathbf{j}$, then $\dot{q}_{E,d}$ and $\dot{q}_{E,s}$ vanish and the electric heat generation reduces to Joule heating $\dot{q}_{E,j} = |\mathbf{j}|^2/\sigma$. The latter condition occurs for example in electroosmosis where the electric current is parallel to the electric double layer [21,29]. It is also interesting to note that the Joule heating term $\dot{q}_{E,j}$ is always positive whereas $\dot{q}_{E,d}$ and $\dot{q}_{E,s}$ can be either positive or negative. In other words, Joule heating is irreversible while $\dot{q}_{E,d}$ and $\dot{q}_{E,s}$ contribute to the reversible heat generation rate. During the charging step, the ions migrated in the direction of decreasing electric potential energy to form the EDLs, releasing thermal energy in the process. During discharging, the ion motion was driven by diffusion and steric effects as the EDLs relaxed. The ion fluxes were then in the direction of increasing electric potential energy and thermal energy was absorbed. To the best of our knowledge, the diffusion and steric contributions $\dot{q}_{E,d}$ and $\dot{q}_{E,s}$ have not been formulated or accounted for in the literature.

Heat of mixing. The heat of mixing term $\dot{q}_S$ is a function of the activity gradients and of the temperature gradient. The activity can

be expressed in terms of the activity coefficient γ_i defined as $a_i = \gamma_i c_i / c_{\text{ref}}$ where c_{ref} is a reference concentration [23]. Then, the heat generation rate $\dot{q}_S$ is given by

$$\dot{q}_S(\mathbf{r},t) = \sum_{i=0}^{n} \mathbf{N}_i \cdot \nabla \left[T^2 R_u \frac{\partial \ln \gamma_i}{\partial T} \right]. \tag{29}$$

Evaluating $\dot{q}_S$ requires an expression for γ_i in terms of the temperature and ion concentrations. For dilute solutions of binary and symmetric electrolytes, the activity coefficient γ_i of ion species i can be expressed, according to the Debye–Hückel limiting law, as [20,23]

$$\ln \gamma_i = -\frac{z^3 e F^2 (c_1 + c_2)^{1/2}}{8\pi (\varepsilon_0 \varepsilon_r R_u T)^{3/2}}. \tag{30}$$

Combining Equations (29) and (30) and assuming that the contribution from the solvent is negligible compared with that of the ions yields $\dot{q}_S = \dot{q}_{S,c} + \dot{q}_{S,T}$ where

$$\dot{q}_{S,c}(\mathbf{r},t) = \frac{3}{32\pi} \frac{z^3 e F^2}{(\varepsilon_0 \varepsilon_r)^{3/2} R_u^{1/2} T^{1/2} (c_1 + c_2)^{1/2}} (\mathbf{N}_1 + \mathbf{N}_2) \cdot \nabla (c_1 + c_2)$$

$$\text{and} \quad \dot{q}_{S,T}(\mathbf{r},t) = -\frac{3}{32\pi} \frac{z^3 e F^2 (c_1 + c_2)^{1/2}}{(\varepsilon_0 \varepsilon_r)^{3/2} R_u^{1/2} T^{3/2}} (\mathbf{N}_1 + \mathbf{N}_2) \cdot \nabla T. \tag{31}$$

In the absence of concentration gradients, $\dot{q}_{S,c}$ vanishes, while $\dot{q}_{S,T}$ vanishes if the temperature is uniform. Here also, $\dot{q}_{S,c}$ and $\dot{q}_{S,T}$ can be either positive or negative and contribute to the reversible heat generation rate. The heat of mixing was previously derived in the form shown in Equation (24) in modeling of transport phenomena in battery systems [25,30]. However, it was typically ignored in solving the energy equation [25,31,32].

Overall, the energy equation can be written as

$$\rho c_p \frac{\partial T}{\partial t} = \nabla \cdot \left(k \nabla T \right) + \dot{q}_{\text{irr}} + \dot{q}_{\text{rev}} \tag{32}$$

where $\dot{q}_{\text{irr}}$ and $\dot{q}_{\text{rev}}$ are the irreversible and reversible heat generation rates, respectively. They are defined as $\dot{q}_{\text{irr}} = \dot{q}_{E,j}$ and $\dot{q}_{\text{rev}} = \dot{q}_{E,d} + \dot{q}_{E,s} + \dot{q}_{S,c} + \dot{q}_{S,T}$. Note that there was no ion insertion into the electrodes [Assumption (1)]. Therefore, the ion fluxes $\mathbf{N}_i$ were equal to zero within the Stern layers. Consequently, the ionic current density and the heat generation rates $\dot{q}_{\text{irr}}(\mathbf{r},t)$ and $\dot{q}_{\text{rev}}(\mathbf{r},t)$ vanished within this compact layer.

3.4.3. Boundary and initial conditions

The one-dimensional transient energy conservation Equation (20) in Cartesian coordinates is a first order PDE in time and second order in space. It is solved in both the Stern and the diffuse layers. It requires one initial condition and two boundary conditions for each layer. The initial temperature was assumed to be uniform and equal to

$$T(x,0) = T_0 \quad \text{for } 0 \le x \le 2L. \tag{33}$$

The surface of electrode A located at $x = 0$ was assumed to be thermally insulated, i.e.,

$$-k \frac{\partial T}{\partial x}(0,t) = 0 \text{ W m}^{-2}. \tag{34}$$

The temperature and heat flux were continuous across the Stern/diffuse layer interface located at $x = H$ such that

$$T(H^-,t) = T(H^+,t) \quad \text{and} \quad -k \frac{\partial T}{\partial x}(H^-,t) = -k \frac{\partial T}{\partial x}(H^+,t). \tag{35}$$

Similarly, the temperature and heat flux were continuous across the second Stern/diffuse layer interface located at $x = 2L - H$, i.e.,

$$T\left(2L - H^-, t\right) = T\left(2L - H^+, t\right) \text{ and}$$
$$-k \frac{\partial T}{\partial x}\left(2L - H^-, t\right) = -k \frac{\partial T}{\partial x}\left(2L - H^+, t\right), \tag{36}$$

The surface of electrode B located at $x = 2L$ was thermally insulated, i.e.,

$$-k \frac{\partial T}{\partial x}(2L,t) = 0 \text{ W m}^{-2}. \tag{37}$$

3.5. Constitutive relationships

The current study focuses on the organic electrolyte consisting of tetraethylammonium tetrafluoroborate ($TEABF_4$) salt in propylene carbonate (PC) solvent. The ions TEA^+ ($i = 1$) and BF_4^- ($i = 2$) have valency $z_1 = -z_2 = 1$ [33–35]. Their effective diameter was taken as $a = 0.68$ nm [33,34]. The dielectric constant, thermal conductivity, density, and specific heat of the electrolyte were taken as those of the PC solvent and equal to $\varepsilon_r = 66.1$, $k = 0.164$ W m^{-1} K^{-1}, $\rho = 1205$ kg m^{-3}, and $c_p = 2141$ J kg^{-1} K^{-1}, respectively [36]. All properties were evaluated at approximately $T_0 = 298$ K. The diffusion coefficient was estimated to be $D = 1.7 \times 10^{-10}$ m^2 s^{-1} using Equation (27) from electrical conductivity data for a concentration of $c_1 = c_2 = c_\infty = 1$ mol L^{-1} [35]. As mentioned previously [Assumption (5)], the present study assumed that the electrolyte properties were independent of temperature T. In keeping with this assumption, the local temperature T in Equations (10), (27) and (31) was evaluated as the initial temperature T_0.

3.6. Method of solution

The one-dimensional governing Equations (3), (9) and (20) and the associated initial and boundary conditions were solved using finite element methods. Numerical convergence was assessed based on the computed local electric potential $\psi(x,t)$, ion concentrations $c_1(x,t)$ and $c_2(x,t)$, and temperature $T(x,t)$. Of these quantities, the temperature was the most sensitive to mesh refinement. The mesh size was the smallest at the Stern/diffuse layer interfaces due to the large potential and concentration gradients and then gradually increased away from these boundaries. The mesh was refined by reducing the element size at the Stern/diffuse layer interface and the maximum element growth rate. The time step was refined by decreasing the relative and absolute tolerances [37]. During each time step, these tolerances were compared with the estimated local error between solutions at the previous and current time steps for each degree of freedom in the model [37]. The time step was then adjusted until the convergence criterion was satisfied, as described in Ref. [37]. This enabled the use of very small time steps during phases with rapid changes, such as the transitions between charging and discharging, while using a larger time step for the rest of the computation. The convergence criteria for the mesh and time step were defined so that the maximum relative difference in the local temperature rise ($T - T_0$) was less than 0.5% when dividing by two (i) the element size at the Stern/diffuse layer interface, (ii) the maximum element growth rate, and (iii) both the relative and absolute tolerances.

4. Results and discussion

The simulations were performed for $c_\infty = 1$ mol L^{-1} of $TEABF_4$ in PC with a domain size of $L = 50$ μm and an initial temperature of $T_0 = 298$ K. The EDLC was cycled at a constant current of $j_s = 14$ mA cm^{-2} with a cycle period $t_c = 0.01$ s. This value of j_s was within the range of current densities per unit separator area reported by experimental studies [4,12]. The combination of j_s and t_c was chosen to yield a realistic maximum potential of 2.5 V chosen by analogy with the operating voltage of many commercial EDLCs using organic electrolytes [27,38].

4.1. Electric potential

Fig. 3(a) shows the electric potential $\psi(0,t)$ at the surface of electrode A as a function of time t corresponding to the total voltage between the electrodes, since electrode B was electrically grounded. Fig. 3(a) shows that the surface potential varied nearly linearly between the minimum potential of 0 V and the maximum potential of 2.5 V. The potential window was determined by the combination of the imposed current density j_s and the cycle period t_c. Note that the planar EDLC simulated charged very rapidly compared to a realistic porous EDLC, so the cycle period t_c corresponding to a realistic current density j_s and realistic potential window of 0–2.5 V was very small.

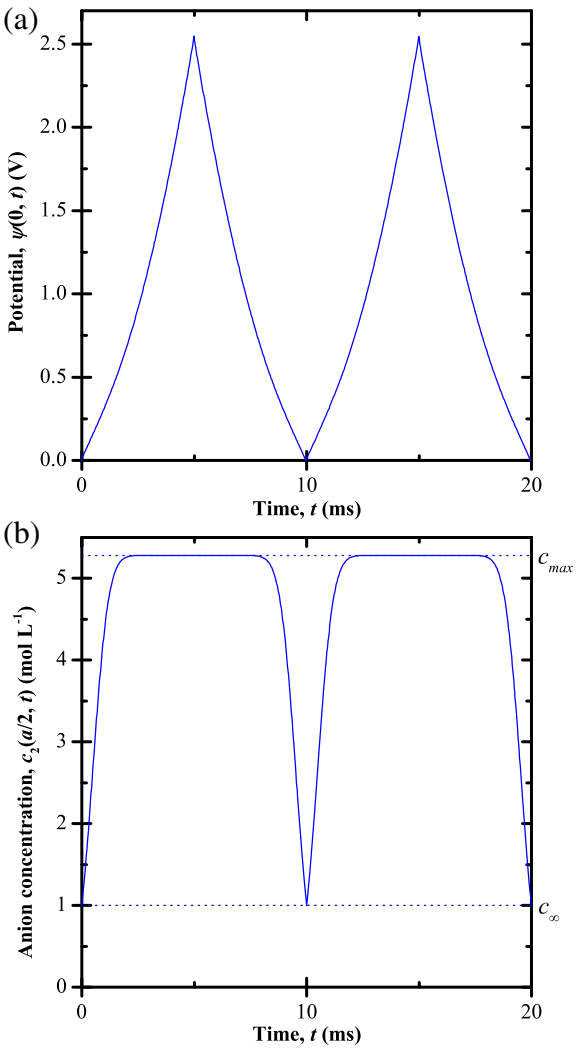

Fig. 3. (a) Electric potential $\psi(0,t)$ at the surface of electrode A and (b) anion concentration $c_2(a/2,t)$ at the Stern/diffuse layer interface as functions of time during two consecutive charging/discharging cycles of period $t_c = 10$ ms under constant current $j_s = 14$ mA cm^{-2}.

4.2. Ion concentrations

Fig. 3(b) shows the anion concentration $c_2(a/2,t)$ at the Stern/diffuse layer interface near electrode A as a function of time t. It shows that the anion concentration at the Stern/diffuse layer interface increased rapidly at the beginning of the charge step. It then leveled off at the maximum concentration $c_{max} = 1/N_A a^3 = 5.3$ mol L^{-1} and remained at this value for most of the cycle. It decreased back to the bulk concentration at the end of the discharge step. The plateau of $c_2(a/2,t)$ corresponded to the surface potential $\psi(0,t)$ exceeding 0.75 V.

Fig. 4 shows the anion concentration $c_2(x,t)$ as a function of location x for several times during a charging step near (a) electrode A and (b) electrode B under constant current $j_s = 14$ mA cm^{-2}. Fig. 4(a) indicates that the anion concentration near electrode A increased from the initial concentration $c_\infty = 1$ mol L^{-1} to c_{max} as the electric double layer formed. After the surface concentration reached c_{max}, a close-packed layer with uniform concentration $c_2 = c_{max}$ formed next to the surface. Beyond the close-packed layer, the concentration decreased to the bulk concentration c_∞ over a narrow region with large concentration gradients. This region will

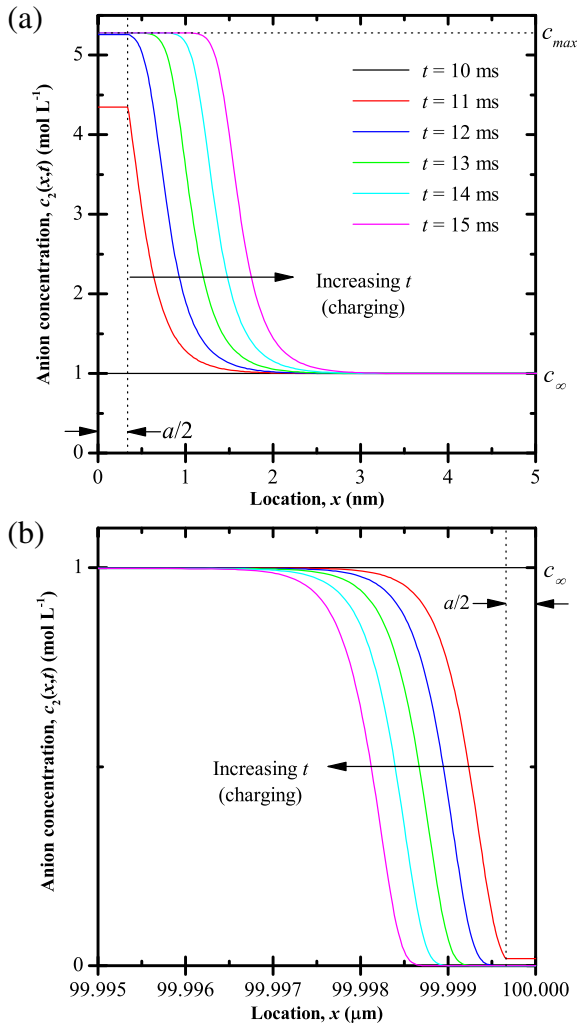

Fig. 4. Predicted anion concentrations $c_2(x,t)$ (a) near electrode A and (b) near electrode B as a function of x at various times during a charging step under constant current $j_s = 14$ mA cm^{-2}.

be referred to as the EDL region. As charging proceeded, the close-packed layer became thicker and the EDL region propagated within the electrolyte in the positive x-direction. By contrast, Fig. 4(b) shows that the anion concentration near electrode B decreased from the initial concentration c_∞ to zero as the EDLC charged. It transitioned from the bulk concentration to zero over a narrow EDL region. As charging proceeded, the EDL region adjacent to electrode B propagated within the electrolyte in the negative x-direction and the region of anion depletion became wider. The cation concentration $c_1(x,t)$ (not shown) was the mirror image of the anion concentration $c_2(x,t)$ such that $c_1(x,t) = c_2(2L - x,t)$.

4.3. Current density

Fig. 5(a) shows the predicted current density $j(L,t)$ at the centerline between electrodes A and B as a function of time t. It demonstrates that the current $\pm j_s$ imposed at electrode A [Equation (5)] resulted in cycles of constant ionic current density of the same magnitude, i.e., $j(L,t) = \pm 14$ mA cm^{-2}. In addition, there was no significant delay between the switching of the imposed current density and the response of the current density $j(L,t)$ at the centerline. Fig. 5(b) shows the current density $j(x,14$ ms$)$ as a function of location x shortly before the end of the charging step. The current density was uniform across the domain, except near the electrodes where it sharply decreased to zero due to the absence of ion insertion. The current density was symmetric about the centerline such that $j(x,t) = j(2L - x,t)$. Similar results were observed at all times.

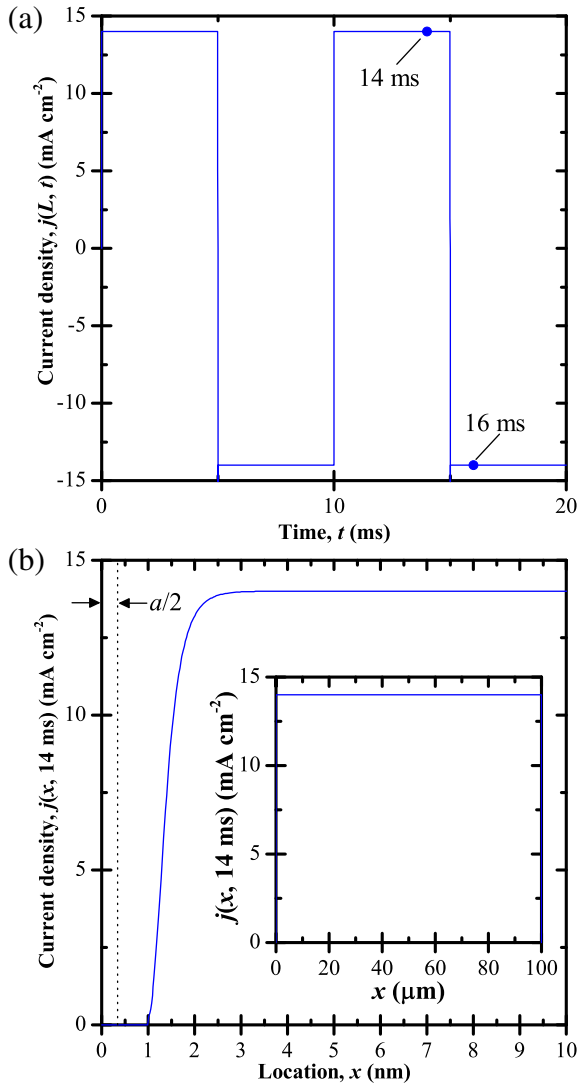

Fig. 5. Predicted current density (a) $j(L,t)$ at the centerline as a function of time t during two consecutive charging/discharging cycles with period $t_c = 10$ ms under constant current $j_s = 14$ mA cm^{-2} and (b) $j(x,14$ ms$)$ as a function of location x at 1 ms before the start of the discharging step.

4.4. Thermal behavior

4.4.1. Local heat generation rates

Fig. 6(a) shows the five heat generation rates $\dot{q}_{E,j}$, $\dot{q}_{E,d}$, $\dot{q}_{E,s}$, $\dot{q}_{S,c}$, and $\dot{q}_{S,T}$ as a function of location x at time $t = 14$ ms shortly before the end of a charging step. The main figure shows the heat generation rates near electrode A while the inset plots them over the entire electrolyte domain. Note that all the heat generation rates were symmetric about the centerline. Fig. 6(a) indicates that $\dot{q}_{E,d}$, $\dot{q}_{E,s}$, and $\dot{q}_{S,c}$ featured large peaks near the electrode surfaces. They were several orders of magnitude larger than $\dot{q}_{E,j}$ within this narrow region but vanished in

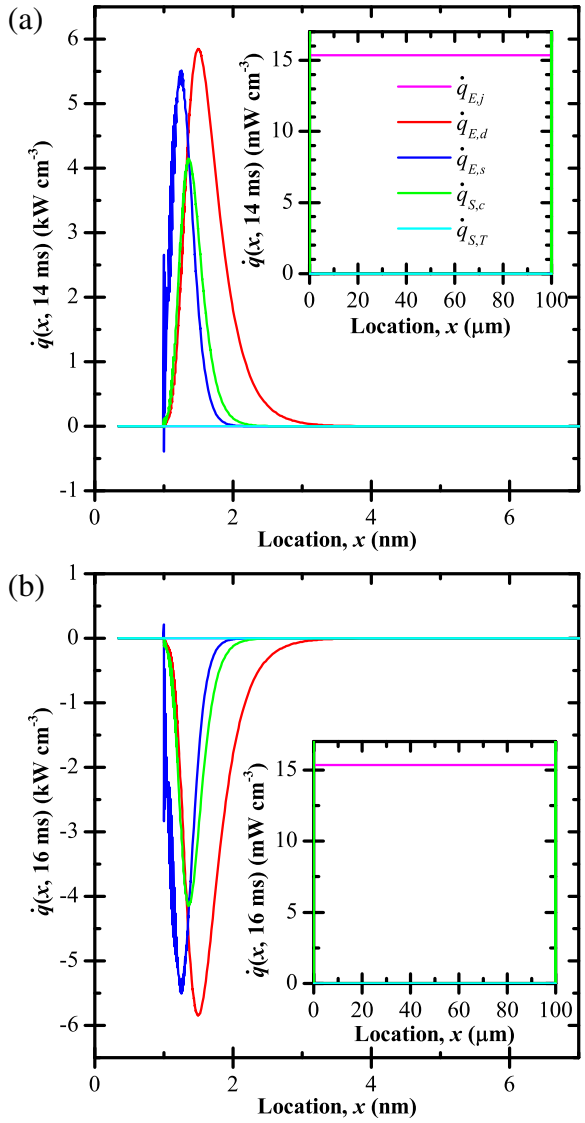

Fig. 6. Predicted heat generation rates $\dot{q}_{E,j}(x,t)$, $\dot{q}_{E,d}(x,t)$, $\dot{q}_{E,s}(x,t)$, $\dot{q}_{S,c}(x,t)$, and $\dot{q}_{S,T}(x,t)$ as a function of location x (a) at time $t = 14$ ms shortly before the end of a charging step and (b) at time $t = 16$ ms shortly after the beginning of a discharging step under constant current $j_s = 14$ mA cm^{-2}.

the rest of the electrolyte domain. The locations of the peaks corresponded to the regions of large concentration gradients shown in Fig. 4. These three terms were positive during the charging step. The inset of Fig. 6(a) shows that the Joule heating term $\dot{q}_{E,j}$ was uniform throughout the electrolyte, equal to $j_s^2/\sigma = 15.3$ mW cm^{-3}, and the only significant heat generation rate beyond the EDL. Indeed, the ionic current density j was uniform and equal to j_s nearly everywhere in the electrolyte [Fig. 5(b)].

Similarly, Fig. 6(b) shows the five heat generation rates $\dot{q}_{E,j}$, $\dot{q}_{E,d}$, $\dot{q}_{E,s}$, $\dot{q}_{S,c}$, and $\dot{q}_{S,T}$ as a function of location x at time $t = 16$ ms shortly after the beginning of the discharging step. This time was chosen because the concentration profiles were almost identical to those at time $t = 14$ ms. Fig. 6(b) indicates that $\dot{q}_{E,d}$, $\dot{q}_{E,s}$, and $\dot{q}_{S,c}$ featured large negative peaks near the electrode surface with identical location and magnitude but opposite sign to those shown in Fig. 6(a). The inset of Fig. 6(b) establishes that $\dot{q}_{E,j}$ remained positive, uniform, and the only significant source of heat generation in most of the electrolyte. Note that $\dot{q}_{S,T}$ was negligible compared to the other heat generation rates over the entire domain and at all times. Therefore, it will be ignored in the rest of this manuscript.

Overall, these results suggest that Joule heating $\dot{q}_{E,j}$ was always positive and corresponded to irreversible heat generation within the electrolyte. By contrast, $\dot{q}_{E,d}$, $\dot{q}_{E,s}$, and $\dot{q}_{S,c}$ could be positive or negative, corresponding to reversible heat generation. However, $\dot{q}_{S,T}$ was negligible compared with the other heat generation rates for the conditions tested. Finally, the total heat generation rate varied strongly with space and time and was not uniform. This is contrary to what is frequently assumed in existing thermal models [5,6,11,13].

4.4.2. Overall heat generation rates

The reversible heat generation rates $\dot{q}_{E,d}$, $\dot{q}_{E,s}$, and $\dot{q}_{S,c}$ locally reached very large magnitudes. However, unlike $\dot{q}_{E,j}$, they were confined to very small regions near the electrode surfaces. To fully assess their relative significance, one should consider their overall contributions integrated over the entire electrolyte domain. The overall heat generation rate per unit separator area (in W m^{-2}) associated with heat generation rate $\dot{q}_i$ is defined as $\dot{Q}_i''(t) = \int_0^{2L} \dot{q}_i dx$. Fig. 7 shows the individual overall heat generation rates as well as the total heat generation rate $\dot{Q}''(t) = \dot{Q}_{E,j}''(t) + \dot{Q}_{E,d}''(t) + \dot{Q}_{E,s}''(t) + \dot{Q}_{S,c}''(t)$ as a function of time. First, it is evident that the irreversible Joule heating $\dot{Q}_{E,j}''$ was positive, constant, and equal to $2Lj_s^2/\sigma = 1.53$ W m^{-2} over the entire simulation time. In addition, the reversible heat generation rates $\dot{Q}_{E,d}''$, $\dot{Q}_{E,s}''$, and $\dot{Q}_{S,c}''$ were positive during charging and negative during discharging, as observed experimentally [12]. Their magnitudes quickly reached a plateau whose duration corresponded to that observed in the concentration at the Stern/diffuse layer interface, i.e., when $c_2(a/2,t) = c_{\max}$ [Fig. 3(a)]. For the conditions tested, this corresponded to a surface potential $\psi(0,t) \geq 0.75$ V. It is interesting to note that EDLCs are often operated between their rated voltage and one-half of their rated voltage, typically 1.25–2.5 V or 1.35–2.7 V for commercial EDLCs with organic electrolyte [3,5,6,13]. Under such conditions, the magnitude of the reversible heat generation rates would remain constant for the entire cycle. Finally, the four heat generation rates considered had the same order of magnitude and all contributed to the total heat generation rate $\dot{Q}''(t)$ in the electrolyte. The largest contribution to the reversible heat generation rate was $\dot{Q}_{E,d}''$, while $\dot{Q}_{E,s}''$ and $\dot{Q}_{S,c}''$ were each approximately half as large as $\dot{Q}_{E,d}''$. The net heat generation over a complete cycle was positive and equal to the irreversible Joule heating $\dot{Q}_{\text{irr}}'' t_c$.

The predicted overall heat generation rates corroborated experimental observations presented in Section 2.3. First, the irreversible heat generation rate $\dot{Q}_{\text{irr}}'' = \dot{Q}_{E,j}'' = 2Lj_s^2/\sigma$ was proportional to j_s^2. In addition, predictions of the overall reversible heat generation rate $\dot{Q}_{rev}'' = \dot{Q}_{E,d}'' + \dot{Q}_{E,s}'' + \dot{Q}_{S,c}''$ at three different current densities (not shown) confirmed that $\dot{Q}_{\text{rev}}''$ was directly proportional to j_s. The reversible heat generation rates were exothermic during charging and endothermic during discharging [4,12].

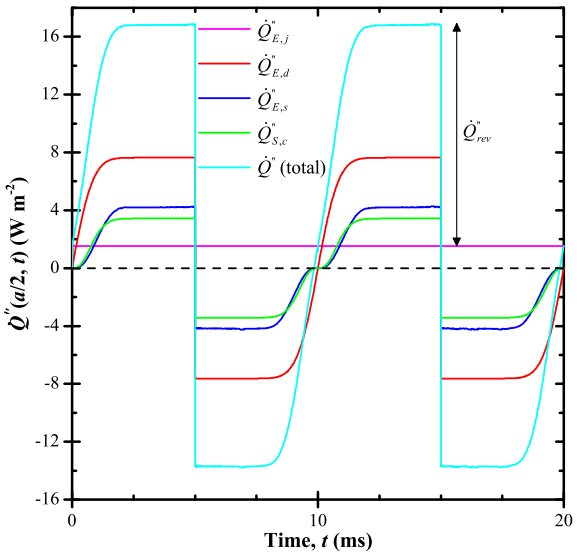

Fig. 7. Predicted overall heat generation rates $\dot{Q}_{E,j}''(t)$, $\dot{Q}_{E,d}''(t)$, $\dot{Q}_{E,s}''(t)$, and $\dot{Q}_{S,c}''(t)$ as well as the total heat generation rate $\dot{Q}''(t)$ as a function of time t.

The overall reversible heat generation rate can alternatively be predicted using Schiffer's model [4] given by Equation (2). On a per unit surface area basis, it yields $\dot{Q}_{\text{rev},S}'' = \dot{Q}_{\text{rev},S}/A = 80.6$ W m^{-2} where A is the electrode surface area. Here, the volumes V_S and V_0 and the current I_s were evaluated as $V_0 = 2LA$, $V_S = aA$, and $I_s = j_s A$, respectively. The predicted value of $\dot{Q}_{\text{rev},S}''$ was approximately five times larger than the plateau obtained numerically as $\dot{Q}_{\text{rev}}'' = 15.3$ W m^{-2}. In the present study, the temperature T_0 and current density j_s were comparable to those used in Refs. [4], but the geometric term $\ln(V_S/V_0)$ was 5–7 times larger. In addition, simulations demonstrated that $\dot{Q}_{\text{rev}}''$ did not change with increasing inter-electrode distance $2L$, provided that the EDLs did not overlap, i.e., $2L \gg 2\lambda_D$. Then, the concentration profiles and resulting $\dot{q}_{\text{rev}}$ within the EDLs remained unchanged. By contrast, Equation (2) predicts increasing values of $\dot{Q}_{\text{rev},S}''$ with increasing L.

4.4.3. Temperature profiles

Fig. 8 shows the predicted temperature change (a) $T(a/2,t) - T_0$ at the Stern/diffuse layer interface and (b) $T(L,t) - T_0$ at the centerline as a function of time t as each contribution $\dot{q}_{E,j}$, $\dot{q}_{E,d}$, $\dot{q}_{E,s}$, and $\dot{q}_{S,c}$ was accounted for sequentially. The Stern/diffuse layer interface $x = a/2$ was very close to the EDL region where the local reversible heat generation rates $\dot{q}_{E,d}$, $\dot{q}_{E,s}$, and $\dot{q}_{S,c}$ were maximum. However, only the Joule heat generation rate $\dot{q}_{E,j}$ was significant at the centerline $x = L$. Both figures indicate that $\dot{q}_{E,j}$ alone would cause the temperature to rise linearly. The addition of the reversible heat generation rates $\dot{q}_{E,d}$, $\dot{q}_{E,s}$, and $\dot{q}_{S,c}$ resulted in temperature oscillations. Furthermore, the increase in oscillation amplitude associated with $\dot{q}_{E,d}$ was approximately twice that associated with either $\dot{q}_{E,s}$ or $\dot{q}_{S,c}$, as expected from their relative magnitudes shown in Fig. 7. Fig. 8(a) shows that the oscillations of $T(a/2,t)$ at the Stern/diffuse layer interface were relatively large. In addition, $T(a/2,t)$ responded quickly to switches from charging to discharging and vice versa. During the first charging step, predictions for $T(a/2,t)$

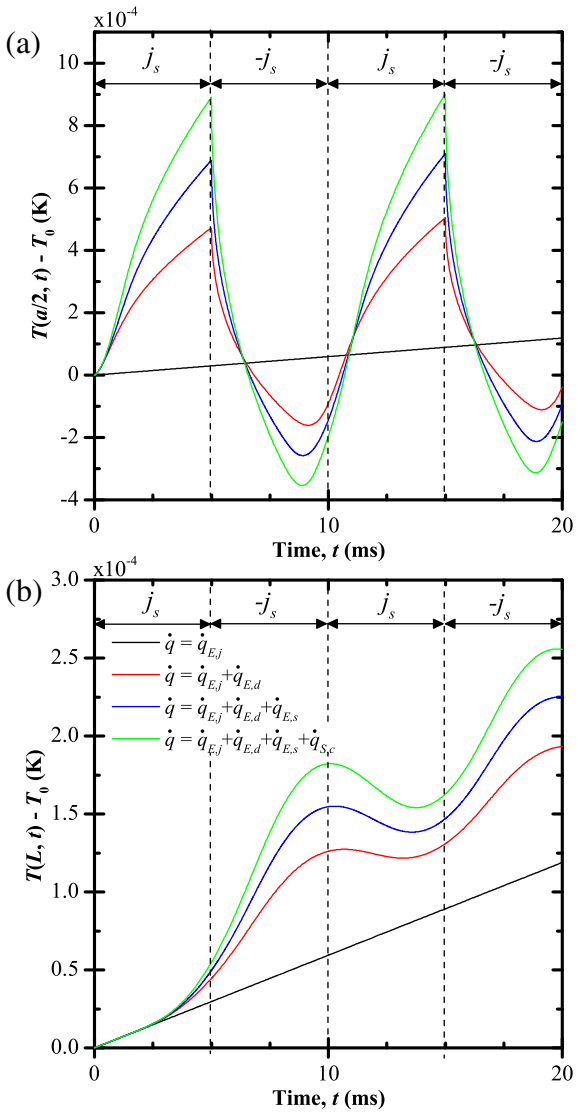

Fig. 8. Predicted temperature change (a) $T(a/2,t) - T_0$ at the Stern/diffuse layer interface and (b) $T(L,t) - T_0$ at the centerline as a function of time t as each individual heat generation rate term was added.

accounting for the reversible heat generation rates diverged immediately from those accounting for Joule heating only. Similarly, $T(a/2,t)$ started to decrease immediately as the discharging step began. By contrast, the response of the centerline temperature $T(L,t)$ showed a delayed response to changes in the reversible heat generation rates occurring near the electrode surface. In particular, $T(L,t)$ diverged only slightly from that predicted using $\dot{q}_{E,j}$ alone through most of the first charging step. Thereafter, the rise and fall of the temperature appeared to be delayed by almost half a cycle period from that predicted at $x = a/2$. In fact, the centerline temperature rose through most of the discharging step and fell through most of the charging step. The oscillations of $T(L,t)$ were also smaller and smoother than those of $T(a/2,t)$. Temperature oscillations at locations between $x = a/2$ and $x = L$ (not shown) were intermediate between those shown in Fig. 8(a) and (b). In particular, the oscillations became smaller, smoother, and more delayed with increasing distance from the electrode surface as the reversible heat generated in the EDL was conducted to the rest of the electrolyte. Finally, Fig. 8(a) shows that the maximum temperature change in the electrolyte was very small. Therefore, neglecting the temperature dependence of the electrolyte properties and of the ion transport (Assumption 5) was appropriate.

4.5. Comparison with experimental temperature measurements

The numerical predictions of the present model were compared qualitatively with experimental temperature measurements reported in the literature [4,13]. Gualous et al. [13] measured the temperature evolution inside and at the outer surface of a 350 F cylindrical EDLC during constant-current cycling at 15 A over the voltage range 1.25 V–2.5 V. The EDLC was cooled by natural convection in air [13]. Similarly, Schiffer et al. [4] measured the temporal evolution of the outer surface temperature of a 5000 F EDLC thermally insulated in a polystyrene box and cycled under a variety of currents and potential windows. The effect of starting the cycle by charging versus discharging was also considered [4].

The numerically-predicted temperature behavior shown in Fig. 8 qualitatively resembled experimental measurements [4,13]. In particular, Gualous et al. [13] measured large and sharp temperature

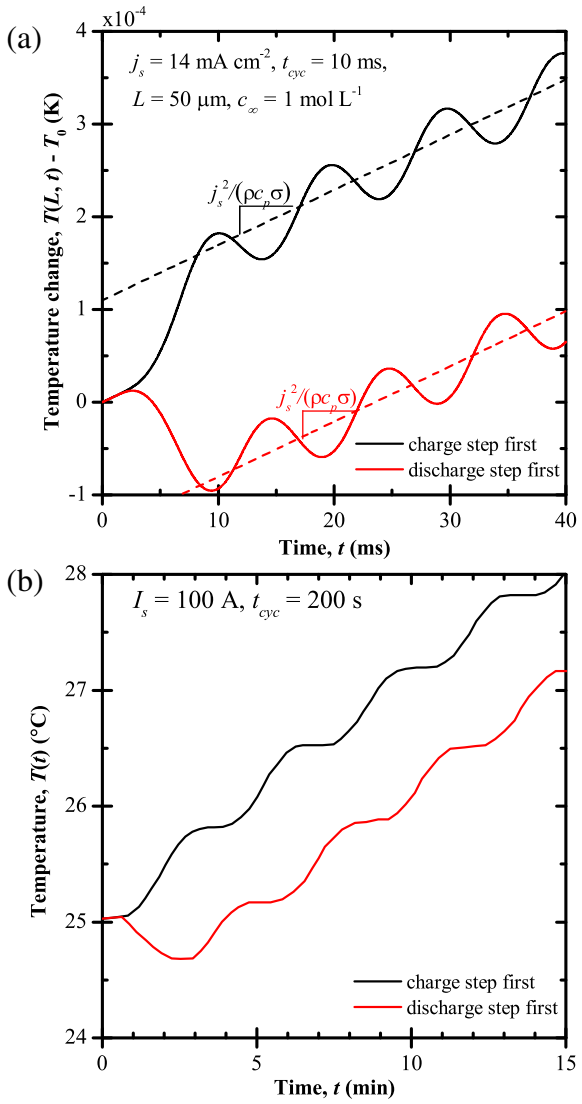

Fig. 9. (a) Numerically predicted temperature change $T(L,t) - T_0$ at the centerline and (b) measured surface temperature of a commercial EDLC (reproduced from Fig. 8 of Ref. [4]) as functions of time t for cases starting with either a charging step or a discharging step.

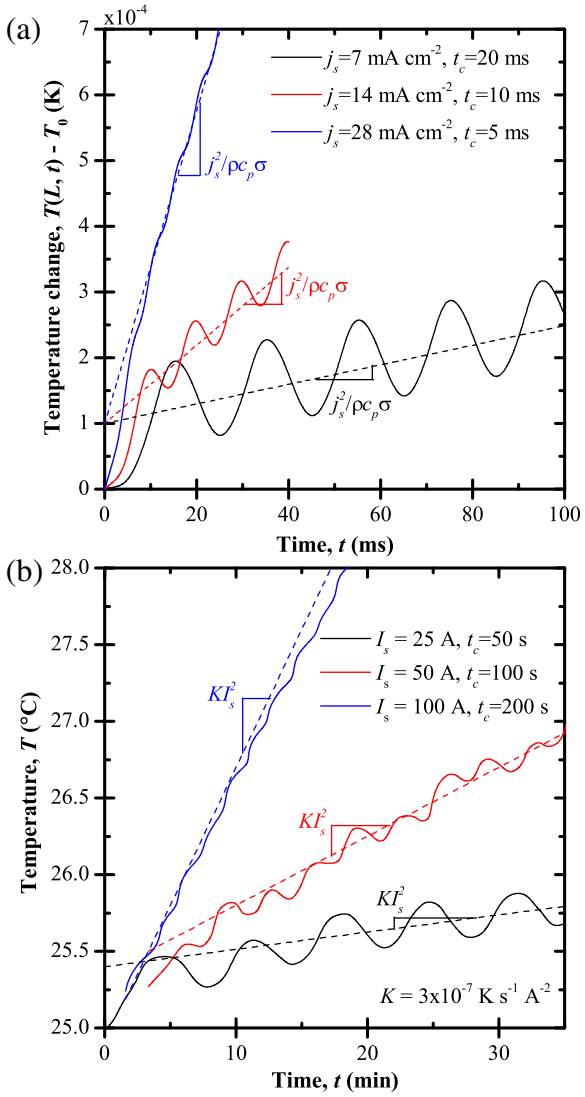

Fig. 10. (a) Predicted temperature rise $T(L,t) - T_0$ at the centerline for cycling at three different current densities j_s over the same potential window and (b) measured surface temperature of a commercial EDLC during cycling under three different values of current I_s over the same potential window (reproduced from Fig. 10 of Ref. [4]) as functions of time t.

oscillations inside an EDLC and smaller and smoother oscillations at the outer surface (Fig. 10 in Ref. [13]).

Fig. 9(a) compares the predicted temperature change $T(L,t) - T_0$ at the centerline as a function of time t for simulations starting with either a charging step or a discharging step. In both cases, the predicted temperature increased linearly for a short period of time ($t < 2.5$ ms) with a slope equal to $\dot{q}_{E,j}/\rho c_p = j_s^2/\sigma\rho c_p$. For the case starting with a charging step under $+j_s$, the temperature continued increasing to reach a peak at $t \approx 10$ ms. However, for the case starting with a discharging step under $-j_s$, the temperature decreased to reach a minimum also around $t \approx 10$ ms. After the first cycle, the temperature in both cases oscillated around an overall temperature rise of slope $\dot{q}_{E,j}/\rho c_p = j^2/\sigma\rho c_p$ corresponding to irreversible Joule heating. Fig. 9(b) shows the measured surface temperature of a commercial EDLC as a function of time t for several charging/discharging cycles starting with either a charging step or a discharging step [4]. It is evident that the predicted thermal behavior shown in Fig. 9(a) was remarkably similar to that observed experimentally. Note that quantitative comparison could not be performed due to the complexity of the porous electrode architecture in the actual EDLC compared with the simple planar electrode simulated. However, the results indicate that our physical model captures the physical phenomena governing the EDLC thermal response during constant-current cycling.

Fig. 10(a) shows the predicted temperature change $T(L,t) - T_0$ at the centerline as a function of time t for cycling at three different current densities j_s. The potential window was held constant as 0–2.5 V by adjusting the cycle period t_c. For all cases, the slope of the overall temperature rise was equal to $j_s^2/\rho c_p \sigma$, corresponding to irreversible Joule heating. Fig. 10(b) shows the measured surface temperatures of a commercial EDLC cycled at three different values of current I_s over the potential window 1.5–2.5 V [4]. Here also, the predicted temporal evolutions of the temperature shown in Fig. 10(a) closely resembled those observed experimentally [4]. However, in both cases, the amplitude of the temperature oscillations decreased with increasing current density. This appears to contradict earlier observations that the reversible heat generation rates increased linearly with increasing current density. However, temperature oscillations predicted near the EDL were significantly larger than those at the centerline and increased with increasing current density (not shown). Thus, the apparent contradiction can be attributed to the fact that the reversible heat generated near the electrode surfaces did not have time to propagate deep into the electrolyte domain due to the reduction in cycle period with increasing current density. Therefore, temperature oscillations at the outer surface of a device behave differently from those near the electrode surface and underestimate the internal temperature oscillations. In fact, the large temperature fluctuations near the electrode create "hot spots" that may contribute to premature degradation of EDLC materials or electrolyte decomposition and of the overall device performance [27].

Finally, Fig. 11 shows the predicted temperature change $T(L,t) - T_0$ at the centerline as a function of time t for cycling at current density $j_s = 14$ mA cm^{-2} over different potential windows, namely 0–2.5 V, 0–1.25 V, and 1.25–2.5 V. It is evident that the temperature rise in these three cases had the same overall slope since the current density j_s was the same for all cases. The largest

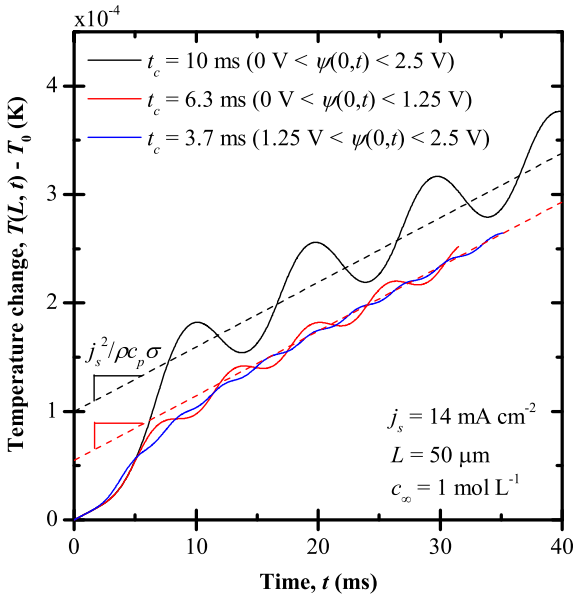

Fig. 11. Predicted temperature rise $T(L,t) - T_0$ as a function of time t at the centerline for cycling at the same current density $j_s = 14$ mA·cm^{-2} over different potential windows.

temperature oscillations were observed for the 2.5 V potential window. Those for the two 1.25 V potential windows were significantly smaller and of similar magnitude to one another. Schiffer et al. [4] reported very similar results for experimental cycling of a commercial EDLC over three analogous potential windows 0.5–2.5 V, 0.5–1.5 V, and 1.5 V–2.5 V.

5. Conclusion

This paper presented a new physical model for coupled ion transport and heat transfer during constant-current charging and discharging of EDLCs. The model accounted for the presence of the Stern layer and for the finite size of ions by using the modified Poisson–Nernst–Planck model. This thermal model is important in that it predicts both the spatial and the temporal variations of the different heat generation rates and of the temperature inside EDLCs based on first principles. Unlike previous thermal models, it accounted for the irreversible Joule heat generation rate $\dot{q}_{E,j}$ as well as three reversible heat generation rates $\dot{q}_{E,d}$, $\dot{q}_{E,s}$, and $\dot{q}_{S,c}$ due to diffusion, steric effects, and entropy changes, respectively. To the best of our knowledge, the present study is the first to derive the diffusion and steric contributions to the heat generation in EDLCs. The reversible heat generation rates were exothermic during charging, endothermic during discharging, and localized in the EDLs. They resulted in large temperature oscillations near the electrodes with maximum temperatures significantly higher than those predicted by Joule heating alone. Predictions of temperature evolution were remarkably similar to those observed experimentally [4,13]. This indicates that the physical model developed captured the physical phenomena governing the thermal behavior of EDLCs.

Acknowledgment

This material is based upon work supported by the National Science Foundation Graduate Research Fellowship under Grant No. DGE-1144087 and as part of the Molecularly Engineered Energy Materials, an Energy Frontier Research Center funded by the U.S. Department of Energy, Office of Science, Office of Basic Energy Sciences under Award Number DE-SC0001342.

References

[1] US Department of Energy, Basic Research Needs for Electrical Energy Storage: Report of the Basic Energy Sciences Workshop for Electrical Energy Storage. Tech. Rep., Office of Basic Energy Sciences, DOE, 2007 http://www.osti.gov/accomplishments/documents/fullText/ACC0330.pdf
[2] P. Guillemet, Y. Scudeller, T. Brousse, Journal of Power Sources 157 (1) (2006) 630–640.
[3] J.R. Miller, Electrochimica Acta 52 (4) (2006) 1703–1708.
[4] J. Schiffer, D. Linzen, D.U. Sauer, Journal of Power Sources 160 (1) (2006) 765–772.
[5] H. Gualous, H. Louahlia-Gualous, R. Gallay, A. Miraoui, IEEE Transactions on Industry Applications 45 (3) (2009) 1035–1044.
[6] M. Al Sakka, H. Gualous, J. Van Mierlo, H. Culcu, Journal of Power Sources 194 (2) (2009) 581–587.
[7] O. Bohlen, J. Kowal, D.U. Sauer, Journal of Power Sources 173 (1) (2007) 626–632.
[8] A. Bard, L. Faulkner, Electrochemical Methods: Fundamentals and Applications, John Wiley & Sons, New York, NY, 2001.
[9] V. Bagotsky, Fundamentals of Electrochemistry, John Wiley & Sons, Hoboken, NJ, 2006.
[10] M.S. Kilic, M.Z. Bazant, A. Ajdari, Physical Review E 75 (2) (2007) 021503.
[11] C. Pascot, Y. Dandeville, Y. Scudeller, P. Guillemet, T. Brousse, Thermochimica Acta 510 (2010) 53–60.
[12] Y. Dandeville, P. Guillemet, Y. Scudeller, O. Crosnier, L. Athouel, T. Brousse, Thermochimica Acta 526 (2011) 1–8.
[13] H. Gualous, H. Louahlia, R. Gallay, IEEE Transactions on Power Electronics 26 (11) (2011) 3402–3409.
[14] C. Zoski (Ed.), Handbook of Electrochemistry, first ed., Elsevier, Oxford, UK, 2007.
[15] M.Z. Bazant, M.S. Kilic, B. Storey, A. Ajdari, Advances in Colloid and Interfacial Science 152 (1–2) (2009) 48–88.
[16] F. Rafik, H. Gualous, R. Gallay, A. Crausaz, A. Berthon, Journal of Power Sources 165 (2) (2007) 928–934.
[17] H. Wang, L. Pilon, Electrochimica Acta 63 (2012) 55–63.
[18] H. Wang, L. Pilon, Electrochimica Acta 64 (2012) 130–139.
[19] R. Hunter, Foundations of Colloid Science, second ed., Oxford University Press, New York, NY, 2001.
[20] J. Newman, Electrochemical Systems, Prentice-Hall, Inc., Englewood Cliffs, NJ, 1973.
[21] R.F. Probstein, Physicochemical Hydrodynamics: an Introduction, second ed., John Wiley & Sons, 2003.
[22] R.B. Bird, Transport Phenomena, John Wiley & Sons, New York, NY, 1962.
[23] T. Engel, P. Reid, Thermodynamics, Statistical Thermodynamics, and Kinetics, second ed., Prentice Hall, Upper Saddle River, NJ, 2010.
[24] F.P. Incropera, D.P. DeWitt, T.L. Bergman, A.S. Lavine, Fundamentals of Heat and Mass Transfer, sixth ed., John Wiley & Sons, Hoboken, NJ, 2007.
[25] W. Gu, C. Wang, Journal of the Electrochemical Society 147 (8) (2000) 2910–2922.
[26] G. Chen, Nanoscale Energy Transport and Conversion, Oxford University Press, New York, NY, 2005.
[27] B. Conway, Electrochemical Supercapacitors: Scientific Fundamentals and Technological Applications, Kluwer Academic/Plenum Publishers, 1999.
[28] G. Tang, C. Yang, J. Chai, H. Gong, International Journal of Heat and Mass Transfer 47 (2) (2004) 215–227.
[29] B.J. Kirby, Micro- and Nanoscale Fluid Mechanics: Transport in Microfluidic Devices, Cambridge University Press, New York, NY, 2010.
[30] D. Bernardi, E. Pawlikowski, J. Newman, Journal of the Electrochemical Society 132 (1) (1985) 5–12.
[31] G.G. Botte, B.A. Johnson, R.E. White, Journal of the Electrochemical Society 146 (1999) 914–923.
[32] L. Rao, J. Newman, Journal of the Electrochemical Society 144 (8) (1997) 2697–2704.
[33] H. Wang, L. Pilon, Journal of Power Sources 221 (2013) 252–260.
[34] J. Chmiola, G. Yushin, Y. Gogotsi, C. Portet, P. Simon, P. Taberna, Science 313 (5794) (2006) 1760–1763.
[35] E.Y. Tyunina, V.N. Afanasiev, M.D. Chekunova, Journal of Chemical and Engineering Data 56 (7) (2011) 3222–3226.
[36] CRC Handbook of Chemistry and Physics, 92nd ed., CRC Press, Boca Raton, FL, 2011.
[37] COMSOL, Inc, COMSOL Multiphysics Reference Guide, 4.2 ed., COMSOL, 2011.
[38] A. Burke, Journal of Power Sources 91 (2000) 37–50.